

Performance Evaluation of a Whole-Body PET Scanner Using the NEMA Protocol

Gunnar Brix, Joachim Zaers, Lars-Eric Adam, Matthias E. Bellemann, Hermann Ostertag, Herbert Trojan, Uwe Haberkorn, Josef Doll, Franz Oberdorfer and Walter J. Lorenz

Research Program Radiological Diagnostics and Therapy, German Cancer Research Center (DKFZ), Heidelberg, Germany

This study evaluates the performance of the newly developed high-resolution whole-body PET scanner ECAT EXACT HR⁺. **Methods:** The scanner consists of four rings of 72 bismuth germanate block detectors each, covering an axial field of view of 15.5 cm with a patient port of 56.2 cm. A single block detector is divided into an 8 × 8 matrix, giving a total of 32 rings with 576 detectors each. The dimensions of a single detector element are 4.39 × 4.05 × 30 mm³. The scanner is equipped with extendable tungsten septa for two-dimensional two-dimensional measurements, as well as with three ⁶⁸Ge line sources for transmission scans and daily quality control. The spatial resolution, scatter fraction, count rate, sensitivity, uniformity and accuracy of the implemented correction algorithms were evaluated after the National Electrical Manufacturers Association protocol using the standard acquisition parameters. **Results:** The transaxial resolution in the two-dimensional mode is 4.3 mm (4.4 mm) in the center and increases to 4.7 mm (4.8 mm) tangential and to 8.3 mm (8.0 mm) radial at a distance of $r = 20$ cm from the center. The axial slice width measured in the two-dimensional mode varies between 4.2 and 6.6 mm FWHM over the transaxial field of view. In the three-dimensional mode the average axial resolution varies between 4.1 mm FWHM in the center and 7.8 mm at $r = 20$ cm. The scatter fraction is 17.1% (32.5%) for a lower energy discriminator level of 350 keV. The maximum true event count rate of 263 (345) kcps was measured at an activity concentration of 142 (26.9) kBq/ml. The total system sensitivity for true events is 5.7 (27.7) cps/Bq/ml. From the uniformity measurements, we obtained a volume variance of 3.9% (5.0%) and a system variance of 1.6% (1.7%). The implemented three-dimensional scatter correction algorithm reveals very favorable properties, whereas the three-dimensional attenuation correction yields slightly inaccurate results in low- and high-density regions. **Conclusion:** The ECAT EXACT HR⁺ has an excellent, nearly isotropic spatial resolution, which is advantageous for brain and small animal studies. While the relatively low slice sensitivity may hamper the capability for performing fast dynamic two-dimensional studies, the scanner offers a sufficient sensitivity and count rate capacity for fully three-dimensional whole-body imaging.

Key Words: PET; NEMA protocol

J Nucl Med 1997; 38:1614–1623

The spatial resolution as well as the axial field of view (FOV) of positron scanners were considerably improved over the last decade to increase the range of applications of PET and its acceptance for studying physiological and biochemical processes in clinical routine. This was mainly achieved by developing whole-body PET systems with smaller detector elements and a much larger number of detector rings. The newly designed whole-body PET system ECAT EXACT HR⁺, manufactured by Siemens/CTI (Knoxville, TN), represents the state of technological development that is commercially available today. This scanner was designed with the intention to: (a) map

regional activity distributions with an almost isotropic spatial resolution of 4–6 mm (FWHM) within a FOV of 20 cm; and (b) compensate the resultant loss in volume sensitivity by detecting all possible lines of response (LORs) between two detectors in any two rings for fully three-dimensional data acquisition and image reconstruction. In this study, the performance of this new system was investigated according to the standards proposed by the National Electrical Manufacturers Association (NEMA) (1,2) using the acquisition parameters recommended by the manufacturer for patient examinations.

Scanner Description

The whole-body scanner ECAT EXACT HR⁺ with a patient port of 56.2 cm consists of four rings of bismuth germanate (BGO) crystal blocks with an inner diameter of 82.7 cm. Each of the 72 blocks per ring is cut into an 8 × 8 array of detector elements with dimensions of 4.39 mm × 4.05 mm × 30 mm (axial × transaxial × depth) separated by small slits of 0.46 mm. The whole system thus consists of 32 detector rings with 576 distinct crystal elements per ring, allowing it to image 63 transaxial slices simultaneously. The maximum FOV is 15.5 cm in the axial direction. To localize an individual event, each block detector is viewed by four photomultiplier tubes, whose output signals are processed by an Anger-type logic to determine in which crystal element the γ -quantum was detected. For two-dimensional data acquisition, tungsten septa can be positioned to align with the tiny gaps between the rings of crystal elements. The interplane septa are 0.8 mm thick and 66.5 mm long. Septa movement can be controlled by the system software.

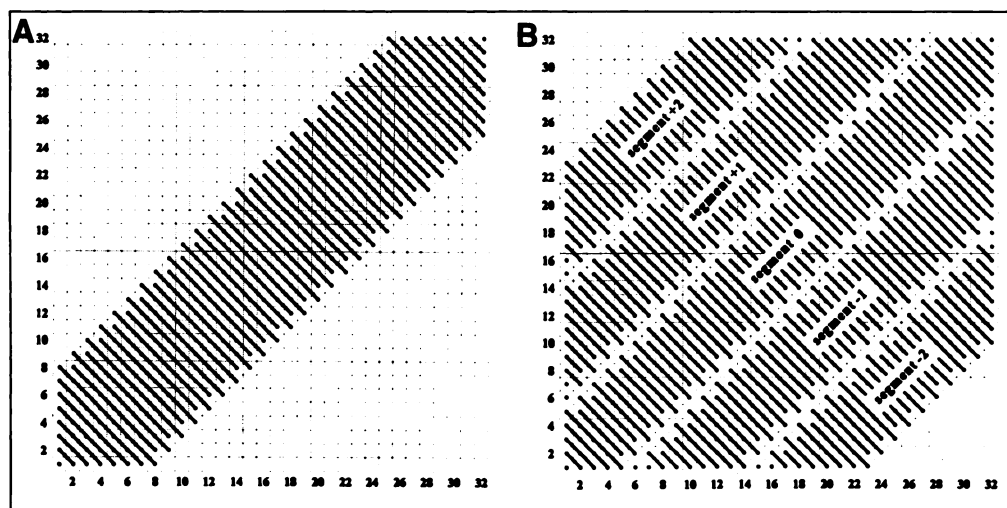
Each block detector output is processed on an analog processor board providing variable front-end preamplification, constant fraction discrimination, position and energy discrimination as well as offset and gain control of the analog-to-digital converters. Energy, position and time information are routed from the bucket controller, serving 12 analog boards, to the coincidence processor generating a 16-bit event-word. This is transferred through fiber optics to the real-time sorter of the advanced computational system (ACS II) housing in a separate cabinet. The resulting sinograms are stored on a separate disk to be accessed for reconstruction by means of SCSI 2.

The ACS II consists of a SPARC CPU driving eight i860 processors (80 MFlops each) and a 128-MB real-time sorter through a VME bus. A scan raw file has 5 MB in the two-dimensional mode and 20 MB in the three-dimensional mode for the default settings for mashing as well as for ring acceptance (see below). The minimum frame time is 3 sec; frames of 7-sec duration can be acquired continuously. Data communication between the ACS II and the workstations for reconstruction and analyzing purposes are provided by means of thin ethernet and standard TCP/IP protocol. The ACS II offers two-dimensional and three-dimensional filtered back-projection reconstruction algorithms using the eight parallel processors. The maximum image matrix is 128 × 128 with an

Received Jun. 27, 1996; revision accepted Nov. 6, 1996.

For correspondence or reprints contact: Gunnar Brix, MD, Forschungsschwerpunkt "Radiologische Diagnostik und Therapie," Deutsches Krebsforschungszentrum, Im Neuenheimer Feld 280, D-69120 Heidelberg, Germany.

FIGURE 1. Michelograms for the standard settings of the ECAT EXACT HR⁺ recommended by the manufacturer for (A) the two-dimensional mode (span = 15, maximum ring difference = 7) and (B) the three-dimensional mode (span = 9, maximum ring difference = 22). Each point denotes a sinogram containing all LORs connecting detectors of two individual rings. Sinograms, which are added up, are connected by a line. Note that the width of a segment is determined by the span.



arbitrary pixel size. A two-dimensional reconstruction for a single frame of 63 slices takes 1.5 min. The resulting image file has a size of 2 MB. The three-dimensional image reconstruction [PROMIS implementation (3)] takes 7 min without and 10 min with three-dimensional scatter correction. These reconstruction times include corrections for normalization, random events, dead-time losses, arc correction, attenuation and activity decay.

To correct for random events, the number of events occurring in a delayed time window with an identical length is measured on-line during data acquisition. These delayed events can be subtracted from the sinograms to compensate for random events detected in the coincidence window. To perform an accurate dead-time correction, the singles rates are directly measured for each detector block. Based on an equation that models the system dead-time, the block singles rates are used to estimate a correction factor on a LOR basis (4). For performing a blank scan required for detector normalization (4) and for acquiring transmission data, the scanner is equipped with three ⁶⁸Ge-rod sources (initial activity: 220 MBq each), which can automatically be extended from lead holders. The rotating rod sources provide for measuring the attenuation coefficients in the two-dimensional mode. For the correction of three-dimensional emission data, attenuation lengths for oblique LORs are obtained by forward projection of the volume defined by the two-dimensional attenuation datasets. Whereas the scatter fraction in the two-dimensional mode is determined and corrected by the well-established convolution-subtraction method (5,6), a simulation-based scatter correction algorithm is applied in the three-dimensional mode using both measured emission and transmission data (7).

Performance Evaluation

Performance measurements and data analysis were done according to the procedures published in the NEMA report NU 2-1994 (2). Although software analysis tools were provided by the manufacturer for this purpose, most of the software used in this study was written by our group to ensure that the guidelines of the NEMA protocol were strictly followed. Before performing the evaluation protocol, a complete normalization of the scanner was done, including: (a) gantry setup to equalize the detector photomultiplier tube gains and energy thresholds, (b) normalization to adjust for relative efficiency variations and (c) activity calibration to make quantitative measurements possible.

For most of the phantom measurements we used a circular Lucite cylinder (inside diameter = 19.4 cm, outside diameter = 20.0 cm, inside length = 19.0 cm), which is capped at one end

using an acrylic lid with provisions for water filling and the interior placement of inserts as defined by the NEMA protocol. The phantom is distributed by PTW (Freiburg, Germany). Line source measurements were performed using a fillable needle of stainless steel with an inside diameter of 1 mm, an outside diameter of 2 mm and a length of 25 cm. Point source measurements, on the other hand, were done using positron emitting ⁶⁴Cu spheres with a diameter of 1 mm, which were produced by neutron activation in the research reactor of our institute. In contrast to fillable spheres, this approach offers two major advantages: (a) ⁶⁴Cu spheres can easily be made with a well-defined geometry and activity and (b) the half-life of ⁶⁴Cu is much longer than that of ¹⁸F (762 versus 109.8 min). All other measurements were performed using the positron emitter ¹⁸F in fluid form of either ionic fluoride (F⁻) or 2-fluorodeoxyglucose (FDG). The lower and upper energy discriminator levels were 350 and 650 keV, respectively. The width of the coincidence window was set to be 12 ns.

All images were reconstructed with the default settings suggested by the manufacturer when nothing else was requested by the NEMA protocol. To reduce the amount of raw data, neighboring LORs were merged into one sinogram. The ECAT software allows a compression in the transaxial (mashing) as well as in the axial direction (spanning). The axial acceptance angle can be parameterized by two variables called span and ring difference. The span factor describes how many individual LORs are added up, while the maximum ring difference defines the maximum number of neighboring rings accepted for coincidence detection. A mash factor of 2, for example, means that 288 projections measured over 180° are reduced to 144 projections, which results in a transaxial sampling angle of 1.2°. A span factor of 15 (9), on the other hand, corresponds to a maximum axial acceptance angle of 4.7° (3.4°). The standard settings of the ECAT EXACT HR⁺ are: mash = 2, span = 15 and maximum ring difference = 7 in the two-dimensional mode as well as mash = 2, span = 9 and maximum ring difference = 22 in the three-dimensional mode. Note that the default three-dimensional mode uses 91% of all possible LORs within the FOV. Following a suggestion of C. Michel (Catholic University of Louvain, Belgium), Figure 1 visualizes the combination of LORs in axial direction in the two-dimensional and three-dimensional mode in the form of two diagrams (Michelograms).

Spatial Resolution

Transverse Resolution (Two-Dimensional and Three-Dimensional). To determine the radial and tangential resolution of the scanner, a line source with an initial ¹⁸F activity of 18.5 MBq

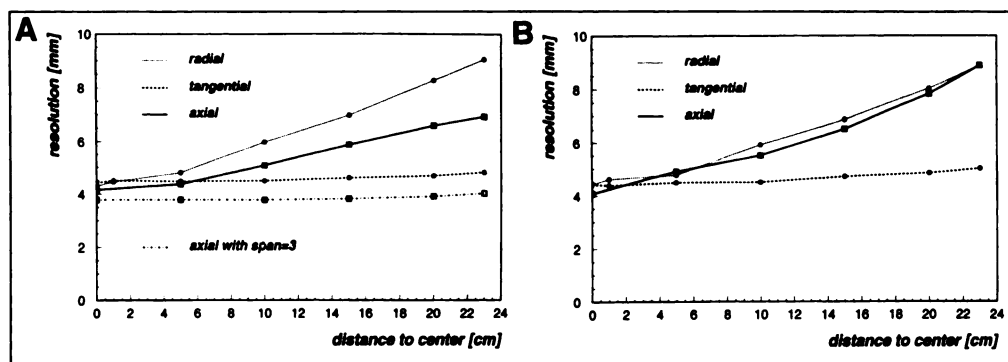


FIGURE 2. Resolution at the FWHM level as a function of the radial distance from the center of the scanner. (A) Transaxial resolution and axial slice width measured in the two-dimensional mode using the default settings for span and ring acceptance. For comparison, the axial slice width measured with a span of three is also plotted. (B) Transaxial and axial resolution measured in the three-dimensional mode using the default settings for span and ring acceptance. For both modes images were reconstructed with a pixel size of $0.506 \times 0.506 \text{ mm}^2$ using a ramp filter with a cutoff at the Nyquist frequency.

was positioned parallel to the axis of the tomograph and measured in air at radial distances of 0, 1, 5, 10, 15, 20 and 23 cm in horizontal as well as in vertical direction. Images were reconstructed with a matrix size of 128×128 and a pixel size of $0.506 \times 0.506 \text{ mm}^2$ using a ramp filter with a cutoff at the Nyquist frequency. Vertical and horizontal profiles through the centers of the activity distribution were determined, and from these the FWHM were estimated both in radial and tangential direction by linear interpolation.

At least 50,000 true events were acquired per slice for both the two-dimensional and three-dimensional measurement condition. The data obtained in the two-dimensional mode are summarized in Figure 2A. The FWHM in tangential direction increases relatively slowly from 4.3 mm at the center to 4.7 mm at a radius of 20 cm, whereas the radial resolution degrades much more to 8.3 mm at a distance of 20 cm. As illustrated in Figure 2B, the results obtained in the three-dimensional mode are quite similar: the FWHM increases in tangential and radial directions from 4.4 mm at the center to 4.8 mm and 8.0 mm, respectively, at a radius of 20 cm.

Axial Slice Width (two-dimensional) and Axial Resolution (three-dimensional). Emission data were acquired at radial point source positions of 0, 5, 10, 15, 20 and 23 cm for both measurement conditions. In the two-dimensional case, a ^{64}Cu point source with an initial activity of 37 MBq was moved in 0.5-mm steps through the axial FOV. The axial slice width (FWHM) was estimated by forming one-dimensional response functions by recording the counts collected for each two-dimensional plane at each axial location of the source. To assess the influence of the chosen span factor on the axial slice width, the two-dimensional measurement was performed twice for a span factor of 15 (standard setting) and 3 (minimum value). In the three-dimensional mode, the spatial resolution (FWHM) in axial direction of stationary point sources placed at axial positions of 0, ± 2 , ± 4 , ± 6 and ± 7 cm was determined from the reconstructed images by forming one-dimensional response functions along profiles through the volume image in the axial direction. Although the axial sampling interval of 2.4 mm is larger than one-third of the expected FWHM of the axial response function, we followed the procedure described in the NEMA protocol. This results in an increased FWHM but reflects exactly the clinical situation.

Because we did not find a significant variation of either the axial slice width or the axial resolution over the axial FOV at the FWHM level, data were averaged over this region. The results obtained at the six radial positions are shown in Figures 2A and 2B for the two-dimensional and three-dimensional mode, respectively. For the standard settings for span and ring acceptance, the axial slice width (two-dimensional mode) increases from 4.2 mm at the center to 6.6 mm at a distance of 20 cm, whereas the axial resolution (three-dimensional mode)

increases from 4.1 mm at the center to 7.8 mm at a radius of 20 cm. The reduction of the span factor in the two-dimensional mode from 15 to 3 results in a nearly constant axial slice width of 3.8 mm.

Scatter Measurement

To characterize the relative system sensitivity to scattered radiation, the scatter fraction SF_i was determined for each slice i by imaging an ^{18}F line source within the water-filled performance phantom in the two-dimensional and three-dimensional mode. The source was positioned parallel to the axis of the cylinder phantom at three radii of 0, 45 and 90 mm. For each radial position, data were acquired over the same time interval and distributed into sinograms. After correction for random coincidences, the total number of events were computed from each sinogram within a fixed radius of 12 cm from the center of the phantom. In a second step, each angular projection in a measured sinogram was shifted so that the pixels containing the maximum values were aligned. Based on these data, the sum of scattered events within a fixed radius of 12 cm from the center of the phantom was estimated. For this purpose, the scattered events under the peak were estimated for each of the three source positions using linear interpolation between the points at ± 2 cm from the source center. From these data, the average scatter fraction for each slice over the whole area of the phantom was computed (cf. Figs. 4-1 and 4-2 in ref. 2) according to

$$SF_i = \frac{\left(\frac{C_{s,i,1}}{A_{ave,1}}\right) + 8\left(\frac{C_{s,i,2}}{A_{ave,2}}\right) + 10.75\left(\frac{C_{s,i,3}}{A_{ave,3}}\right)}{\left(\frac{C_{TOT,i,1}}{A_{ave,1}}\right) + 8\left(\frac{C_{TOT,i,2}}{A_{ave,2}}\right) + 10.75\left(\frac{C_{TOT,i,3}}{A_{ave,3}}\right)}, \quad \text{Eq. 1}$$

where $C_{TOT,i,k}$ and $C_{s,i,k}$ are the number of total and scattered counts in sinogram i ($1 \leq i \leq 63$ (239) in the two-dimensional/ (three-dimensional mode), respectively, and $A_{ave,k}$ is the average radioactivity during the acquisition time interval for the line source at position k ($k = 1, 2, 3$).

Using initial activities of $A_0 = 17.9 \text{ MBq}$ for the two-dimensional measurement and $A_0 = 2.2 \text{ MBq}$ for the three-dimensional measurement, more than 200,000 counts were detected in each sinogram with dead-time losses below 5% of the total event rate. In both cases, however, the random coincidence rate significantly exceeded the prescribed limit of 5% of the total event rate at the beginning of the acquisition period (two-dimensional mode, 10.9%; three-dimensional mode, 20.0%). Figure 3 shows the scatter distribution function of the line source in the center of the water-filled phantom measured in the two-dimensional and three-dimensional mode. Figure 4 demonstrates the variation of the scatter fraction for the 63 sinograms measured in the two-dimensional mode and

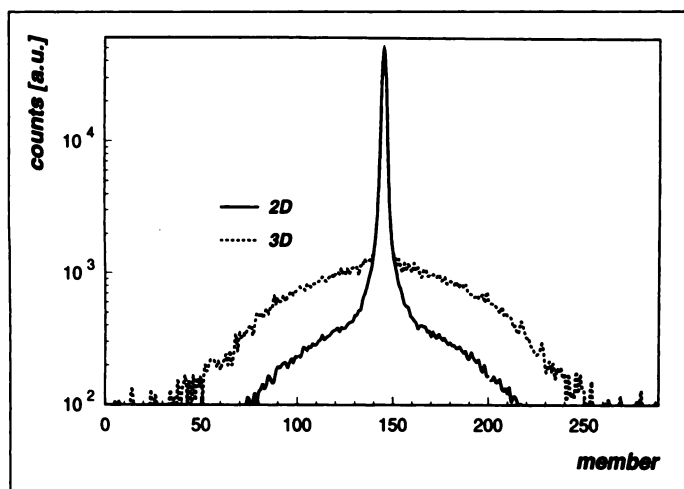


FIGURE 3. Scatter distribution function of a line source in the center of the water-filled performance phantom measured in the two-dimensional and three-dimensional mode.

for the 63 nonoblique sinograms (central segment of the Michelogram, cf. Fig. 1B) measured in the three-dimensional mode. Averaging the scatter fraction over all sinograms yields a value of $SF = 17.1 \pm 3.0\%$ for the two-dimensional mode, which increases to SF in the three-dimensional mode.

Count Losses and Random Measurements

To characterize the count rate behavior of the tomograph for a wide range of scanning conditions, losses of events due to dead-time and randoms were measured as a function of activity level. For this purpose, the performance phantom was loaded with an initially high ^{18}F activity diluted in deaerated water and dynamically scanned in two-dimensional as well as three-dimensional mode. In each mode, total and random events were measured independently and stored in separate sinograms. From the uncorrected sinogram data, the total count rate $R_{\text{tot},i,j}$, the random count rate $R_{\text{r},i,j}$, the true count rate $R_{\text{t},i,j} = (R_{\text{tot},i,j} - R_{\text{r},i,j})(1 - SF_i)$ and the extrapolated count rate $R_{\text{extr},i,j}$ (extrapolated from low count rate data) were computed for each slice i and each frame j within a rectangular region of interest (ROI) of width 240 mm and spanning all angles. These values were summed over all slices to obtain the corresponding system

count rates $R_{\text{tot},\text{sys},j}$, $R_{\text{r},\text{sys},j}$, $R_{\text{t},\text{sys},j}$ and $R_{\text{extr},\text{sys},j}$, as well as the system percent dead-time

$$\text{PDT}_{\text{sys},j} = 100 - 100 \left(\frac{R_{\text{tot},\text{sys},j} - R_{\text{r},\text{sys},j}}{R_{\text{extr},\text{sys},j}} \right). \quad \text{Eq. 2}$$

For the two-dimensional and three-dimensional measurements the phantom was initially filled with 315 kBq/ml and 117 kBq/ml of ^{18}F , respectively, and scanned over a period of more than 11 half-lives. In both cases, the activity injected into the phantom was determined with a calibrated ionization chamber. The estimated system count rates are plotted in Figure 5 as a function of the average activity concentration. Figure 6 presents the behavior of the system dead-time. The relevant performance parameters estimated from these curves are summarized in Table 1.

Sensitivity Measurement

The sensitivity measurement is designed to measure the mean sensitivity per image plane before any corrections for variations in detector sensitivity have been applied (sensitivity test) and to characterize the uniformity of sensitivity in the axial direction (relative sensitivity profile test).

Sensitivity Test (Two-Dimensional and Three-Dimensional). The sensitivity test is based on the true count rate data acquired at low activity levels in the count rate measurements (see above) after random and dead-time corrections. The slice sensitivities S_i for unscattered events were estimated by the equation:

$$S_i = \frac{C_{i,\text{TOT},120\text{mm}}}{T_{\text{acq}}} \left(\frac{1 - SF_i}{a_{\text{ave}}} \right), \quad \text{Eq. 3}$$

where $C_{i,\text{TOT},120\text{mm}}$ is the total number of true counts in slice i within a radius of 120 mm, a_{ave} is the average activity concentration in the phantom during the acquisition time interval T_{acq} , and SF_i is the corresponding scatter fraction determined according to Equation 1.

Plots of the evaluated two-dimensional and three-dimensional slice sensitivity values S_i are shown in Figure 7. The slice sensitivity is quite uniform over the central slices (nos. 11–53). Averaging the S_i values over these slices results in a mean slice sensitivity of (0.097 ± 0.006) cps/Bq/ml. The total system sensitivity for true events, i.e., the sum of overall measured S_i values, is 5.7 cps/Bq/ml. In the three-dimensional mode, the system sensitivity increases to 27.7 cps/Bq/ml, which is a factor of about 4.9 higher than the corresponding two-dimensional value. It should be recognized that the default three-dimensional mode uses only 91% of all possible LORs within the FOV. As expected, the estimated two-dimensional and three-dimensional system sensitivities agree with the gradient of the true count rate curve at very low activity values (cf. Fig. 5).

Relative Sensitivity Profile Test (Two-Dimensional). This test is based on the data from the axial slice width measurements (see above), which were performed by moving a ^{64}Cu point source in 0.5-mm steps along the axis of the scanner. The central part of the axial sensitivity profile, i.e., the combination of all axial response functions normalized to the slice sensitivity S_i calculated above, is plotted in Figure 8. The whole profile was analyzed to determine the peak-to-valley ratio PV_i for each valley i ($1 \leq i \leq 62$) by

$$PV_i = \frac{\text{Max}_{\text{L},i} + \text{Max}_{\text{R},i}}{2 \text{Min}_i}, \quad \text{Eq. 4}$$

where $\text{Max}_{\text{L},i}$ and $\text{Max}_{\text{R},i}$ are the maximum values of two neighboring slices (when the source is closely aligned with the

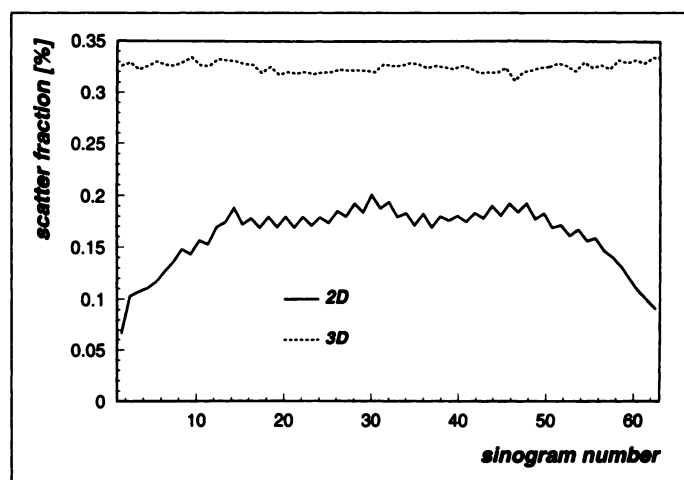
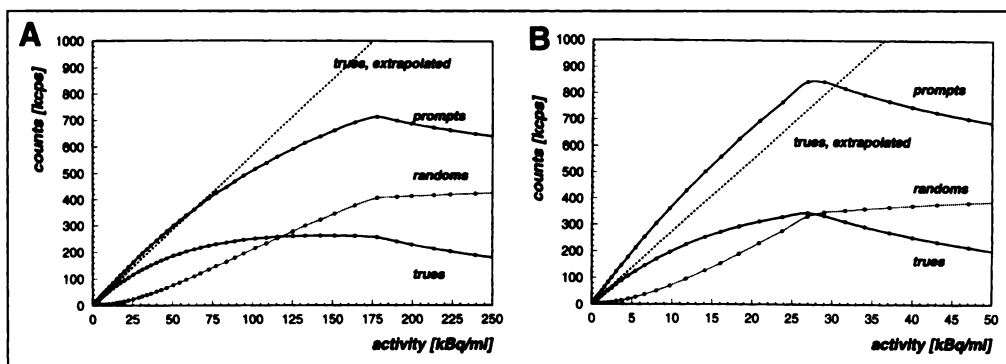


FIGURE 4. Variation of the scatter fraction for the 63 sinograms measured in the two-dimensional mode and for the 63 nonoblique sinograms (central segment of the Michelogram, see Fig. 1B) measured in the three-dimensional mode. In the two-dimensional mode, the cross planes have a slightly higher scatter fraction than the direct planes. This effect vanishes in the three-dimensional mode. The scatter fractions estimated in the three-dimensional mode from the oblique sinograms are slightly smaller than the data shown.

FIGURE 5. System count rate behavior determined in (A) two-dimensional mode and (B) three-dimensional mode as a function of the activity concentration. In both cases, total, random, true and extrapolated count rates are presented. The relevant performance parameters estimated from these plots are summarized in Table 1. Note that the count rates were summed over a rectangular ROI centered over the radial axis of the sinograms (width = 240 mm).



center of each slice) and Min_i is the minimum value (when the source is between the two slices). From the PV_i ratios, which are plotted in Figure 9 for all valleys, a mean peak-to-valley ratio of $\text{PV}_{\text{ave}} = 1.31 \pm 0.05$ was calculated.

Uniformity Measurements

For the uniformity test, the performance phantom was filled with ^{18}F radioactivity diluted in deaerated water and centered axially in the FOV but displaced vertically 25 mm off axis to reduce the scanning symmetry. Images were reconstructed with all corrections using the two-dimensional and three-dimensional standard parameters described above. To eliminate potential effects of measured attenuation correction data, attenuation correction was done analytically with the known attenuation coefficient of water ($\mu = 0.095 \text{ cm}^{-1}$). For the quantitative evaluation, a map of contiguous $8.1 \times 8.1 \text{ mm}^2$ square regions fully inscribed into a circle of 175 mm in diameter was placed over the phantom image (cf. Fig. 7-1 in ref. 2). Based on this spatial subdivision, maximum and minimum nonuniformities (NU), as well as the coefficient of variation (CV), were determined according to

$$\text{NU}_i^{\text{Max}} = \frac{\text{Max}(C_k) - \text{Ave}(C_k)}{\text{Ave}(C_k)} \quad \text{Eq. 5a}$$

$$\text{NU}_i^{\text{Min}} = \frac{\text{Min}(C_k) - \text{Ave}(C_k)}{\text{Ave}(C_k)} \quad \text{Eq. 5b}$$

$$\text{CV}_i = \frac{1}{\text{Ave}(C_k)} \sqrt{\frac{1}{K-1} \sum_{k=1}^K (C_k - \text{Ave}(C_k))^2} \quad \text{Eq. 5c}$$

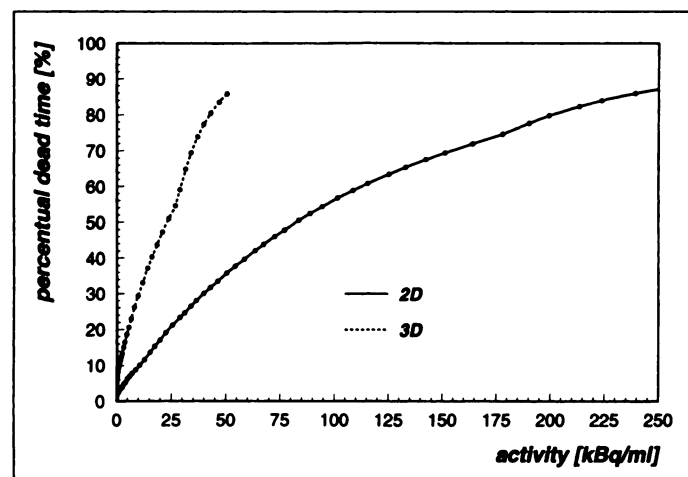


FIGURE 6. System dead-time behavior in two-dimensional and three-dimensional mode as determined from the count rate plots shown in Figure 5.

$\text{Max}(C_k)$ is the maximum number of counts, $\text{Min}(C_k)$ is the minimum number of counts and $\text{Ave}(C_k)$ is the average number of counts with respect to any square region k within a given slice i ($1 \leq i \leq 63$, slice uniformity) or within the entire FOV (volume uniformity). To examine the interslice uniformity, system uniformity data were determined according to Equations 5a–c, where C_k denotes now the average number of counts in slice k ($1 \leq k \leq 63$).

The uniform activity distribution was scanned in the two-dimensional and three-dimensional mode over a period of 10 hr leading to a total of 1.50×10^9 and 2.00×10^9 net true events, respectively. For both measurement conditions, the random fraction (two-dimensional, 36%; three-dimensional, 22%) exceeded the recommended limit of 20%. The slice uniformity data obtained in the two-dimensional and three-dimensional mode are plotted in Figure 10, whereas the computed volume and system uniformity data are summarized in Table 2. They reveal that there are no systematic nonuniformities over the central slices (nos. 11–53). The estimated values seem to simply reflect the overall statistical uncertainty.

Accuracy: Scatter Correction

To assess the accuracy of the scatter correction technique incorporated in the scanner software, a 50-mm diameter cylinder insert was placed 60 mm offset from the axis of the phantom. The main compartment of the phantom was loaded with a low amount of ^{18}F activity, whereas the hollow insert was filled with nonradioactive water. To reduce the scanning

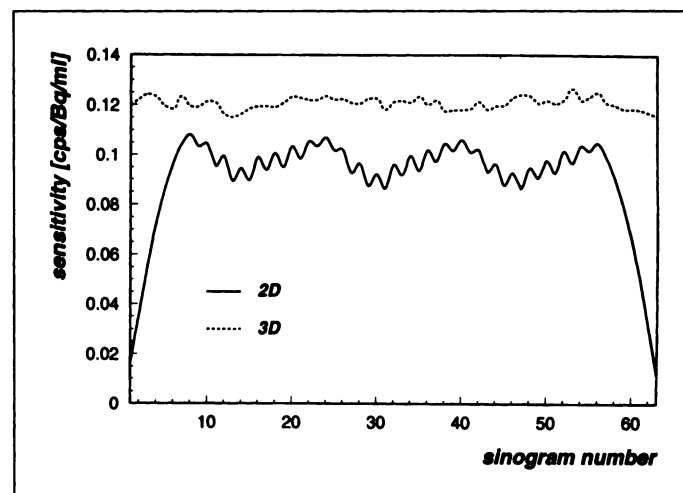


FIGURE 7. Variation of the sensitivity for the 63 sinograms measured in the standard two-dimensional mode and for the 63 nonoblique sinograms (central segment of the Michelogram) measured in the standard three-dimensional mode. In the three-dimensional mode, the total number of sinograms is 239 (see Fig. 1B) resulting in a much higher total system sensitivity as compared with the two-dimensional mode.

TABLE 1
Count Rate Performance Parameters

| Scan Mode | 50% dead-time | | Peak of true rate | | True rate = random rate | |
|-------------------|--------------------|-------------------|--------------------|-------------------|-------------------------|-------------------|
| | a_{ave} (kBq/ml) | Trues rate (kcps) | a_{ave} (kBq/ml) | Trues rate (kcps) | a_{ave} (kBq/ml) | Trues rate (kcps) |
| Two-dimensional | 83.6 | 237 | 142 | 263 | 121 | 259 |
| Three-dimensional | 23.7 | 330 | 26.9 | 345 | 27.9 | 339 |

symmetry, the phantom was placed 2.5 cm vertically off center. Image data were measured and reconstructed with all corrections using the standard two-dimensional and three-dimensional acquisition parameters mentioned above. Again, an analytical attenuation correction was applied with an attenuation coefficient of $\mu = 0.095 \text{ cm}^{-1}$. In each reconstructed image plane 12 ROIs were defined each 30 mm in diameter. One ROI was centered over the cold insert region, whereas the other 11 ROIs were placed in the background area (cf. Fig. 8-1 in ref. 2). For each slice i ($1 \leq i \leq 63$), the remnant scatter fraction in the cold area after scatter correction was defined by

$$\Delta SF_{\text{corr},i} = \frac{C_{\text{cyl},i}}{C_{\text{ave},i}}, \quad \text{Eq. 6}$$

where $C_{\text{cyl},i}$ is the number of counts in the ROI inside the insert and $C_{\text{ave},i}$ is the average number of counts in the other 11 ROIs.

On average, more than 2 million counts per image plane were acquired in the two-dimensional mode (1.50×10^8 total net true events in 63 image planes) as well as in the three-dimensional mode (1.71×10^8 total net true events) by scanning over a period of 12 hr. The random fraction (two-dimensional, 5.2%; three-dimensional, 13.7%) exceeded the recommended limit of 5% in both cases. The results are summarized in Figure 11. In the two-dimensional mode, the mean remnant scatter fraction was found to be $3.2 \pm 2.9\%$. In the three-dimensional mode, the scatter correction was even better, yielding a mean value of $-0.2 \pm 3.5\%$. For comparison, without scatter correction, we estimated a scatter fraction of $10.3 \pm 2.8\%$ in the two-dimensional mode and of $23.9 \pm 2.6\%$ in the three-dimensional mode. The data reveal that the scatter fraction in the two-dimensional mode is slightly underestimated by the implemented convolution-subtraction algorithm, whereas the analytical three-dimensional scatter correction algorithm yields excellent results for this experimental setup.

Accuracy: Count Rate Correction

To evaluate the accuracy of corrections for dead-time losses and random events, the performance phantom was loaded with an initially high ^{18}F activity diluted in deaerated water and dynamically scanned in the two-dimensional as well as in the three-dimensional mode. Images were reconstructed from the measured sinogram data with all corrections applied using the standard reconstruction parameters. For each slice i and each frame j , the true count rate $R_{\text{ROI},i,j}$ was determined within a circular ROI of 180 mm in diameter centered on the image of the phantom. Based on these data, the relative count rate error

$$\Delta r_{i,j} = \frac{R_{\text{Ext},i,j} - R_{\text{ROI},i,j}}{R_{\text{Ext},i,j}} \quad \text{Eq. 7}$$

was calculated, where $R_{\text{Ext},i,j}$ is the extrapolated true count rate determined from low count rate data.

For the two-dimensional and three-dimensional measurements, the phantom was initially filled with 1.5 GBq and 210 MBq of ^{18}F , respectively. The activity concentrations were determined from samples with help of an automated NaI(Tl) well counter. The highest and lowest values of $\Delta r_{i,j}$ among the slices i are plotted in Figure 12 versus the average activity concentration for the two-dimensional and three-dimensional mode. To characterize the performance of the system, the bias among the slices was estimated by linear interpolation at activity concentrations at which the percent dead-time is 50% (see Table 1). At these activity levels, the relative count rate error lies between -2.8% and 6.0% (system value: 0.7%) in the two-dimensional mode and between -3.1% and 6.4% (system value: -0.3%) in the three-dimensional mode.

Accuracy: Attenuation Correction

Attenuation correction is the largest correction performed in whole-body PET. Its accuracy was studied using the performance phantom with three inserts (50 mm in diameter) filled

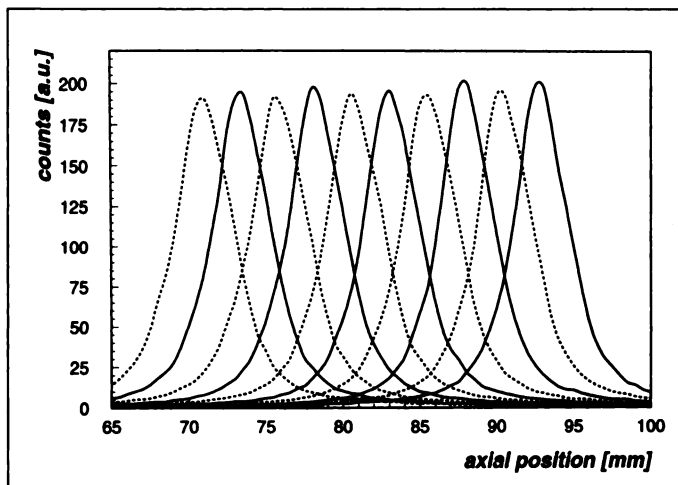


FIGURE 8. Axial sensitivity profile obtained from 10 representative response functions determined in the middle of the axial FOV after normalization to the slice sensitivity.

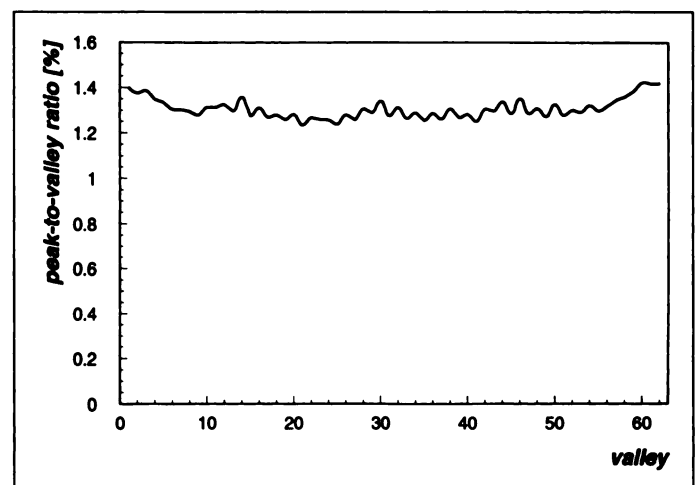
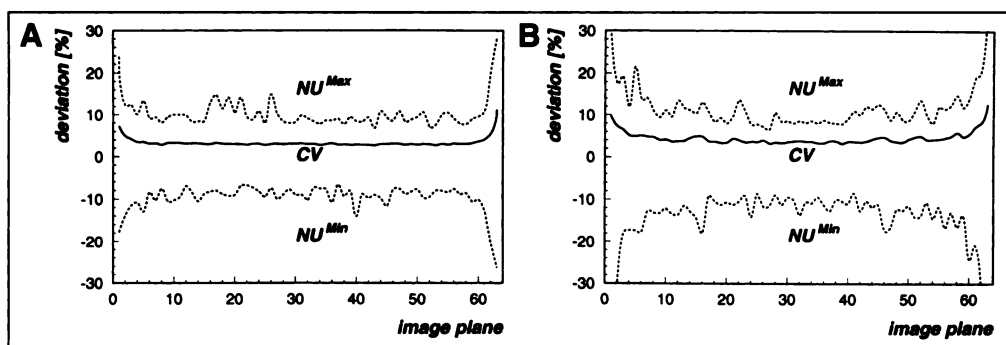


FIGURE 9. Peak-to-valley ratios as a function of valley number. Data are determined from the axial sensitivity profile shown in Figure 8 and characterize the uniformity of sensitivity in the axial direction.

FIGURE 10. Slice uniformity data obtained in (A) two-dimensional mode and (B) three-dimensional mode. Plotted are the minimum (NU^{Min}) and maximum (NU^{Max}) nonuniformities, as well as the coefficient of variation (CV) for all image planes (c.f. Eqs. 5a-c). The volume and system uniformity values are summarized in Table 2.



with air (lungs), water (tissue) and Teflon (bone). For the emission measurement, the water-filled main compartment of the test phantom was loaded with a ^{18}F solution. After positioning the phantom 2.5 cm vertically off center, data were acquired in the two-dimensional as well as in the three-dimensional mode. After the activity had decayed, the acquisition of the transmission and blank scan was performed using the method recommended by the manufacturer for patient studies. In the transmission corrected emission images, three circular ROIs of 30 mm in diameter were defined on the air, water and solid insert, respectively, and nine ROIs with an identical size in the uniform activity area (cf. Fig. 10-2 in ref. 2). For each insert, the remnant attenuation error was calculated in each of the slices i ($1 \leq i \leq 63$) by

$$\Delta C_{insert,i} = \frac{C_{insert,i}}{C_{N,i}}, \quad \text{Eq. 8}$$

where $C_{insert,i}$ is the number of counts in the ROI over the insert and $C_{N,i}$ is the average number of counts in the nine background ROIs. In addition, the nonuniformity of the attenuation correction was characterized for each slice i by the parameters

$$NU_{A,i}^{Max} = \frac{\text{Max}(C_{k,i}) - C_{N,i}}{C_{N,i}} \quad \text{Eq. 9a}$$

$$NU_{A,i}^{Min} = \frac{\text{Min}(C_{k,i}) - C_{N,i}}{C_{N,i}}, \quad \text{Eq. 9b}$$

where $C_{k,i}$ is the number of counts in the k th background ROI ($1 \leq k \leq 9$), and $C_{N,i}$ is their average value.

On average, more than 2 million counts per image plane were detected in the two-dimensional mode (1.50×10^8 total net true events) as well as in the three-dimensional mode (1.33×10^8 total net true events) by scanning over a period of 10 hr. The random fraction (two-dimensional, 5.6%; three-dimensional, 17.3%) exceeded the recommended limit of 5% in both cases. The transmission scan was acquired (more than 10 half-lives after the measurement of the emission data) in the two-dimensional mode over a period of 20 min resulting in 2.87×10^8 total net true events. For the three-dimensional

attenuation correction, a measured two-dimensional transmission scan was transformed to a three-dimensional attenuation dataset. The remnant attenuation errors estimated for the three inserts are plotted for each image plane in Figure 13 for the two-dimensional as well as three-dimensional mode. Averaging the remnant attenuation errors overall slices i yielded: $\Delta C_{air} = 6.3 \pm 1.7\%$, $\Delta C_{water} = 3.6 \pm 3.4\%$ and $\Delta C_{solid} = 4.6 \pm 4.0\%$ in the two-dimensional mode and $\Delta C_{air} = 13.3 \pm 2.7\%$, $\Delta C_{water} = -0.6 \pm 5.4\%$ and $\Delta C_{solid} = -13.3 \pm 8.9\%$ in the three-dimensional mode. The maximum and minimum nonuniformity values of the system in the two-dimensional mode, defined as the mean values of $NU_{A,i}^{Min}$ and $NU_{A,i}^{Max}$ overall slices i , were $-6.7 \pm 1.9\%$ and $6.2 \pm 2.6\%$, respectively. The corresponding three-dimensional values were found to be $-7.3 \pm 4.6\%$ and $6.5 \pm 3.5\%$. The attenuation errors estimated in the two-dimensional mode appear to simply reflect the remnant scatter fraction (see above), whereas the three-dimensional attenuation correction results in systematic errors in low (lungs) and high (bone) density regions.

Clinical Imaging

To demonstrate the image quality obtainable in oncological patient examinations, Figure 14 shows a coronal projection image and a sagittal emission scan of a female patient with follicular thyroid carcinoma (pT2NxMx) 2 yr after surgical resection and two radioiodine therapies with 8 GBq ^{131}I total dose. The patient presented with raising plasma thyroglobulin levels. At our institute, as at most other sites, whole-body PET studies were mostly performed without attenuation correction to limit the total scan time to about 1 hr and to reduce the exposure to ionizing radiation. Thus, 40 min after injection of 460 MBq $[^{18}F]FDG$, the patient was scanned at five axial positions of the FOV with an overlap of five planes. At each axial position,

TABLE 2
Performance Parameters (see Eqs. 5a-c)
Characterizing Volume and System Uniformity

| | NU^{Min} (%) | NU^{Max} (%) | CV (%) |
|------------------------|----------------|----------------|--------|
| two-dimensional mode | | | |
| volume | -31.5 | 26.5 | 3.9 |
| system | -7.1 | 3.3 | 1.6 |
| three-dimensional mode | | | |
| volume | -57.0 | 48.8 | 5.0 |
| system | -3.4 | 5.3 | 1.7 |

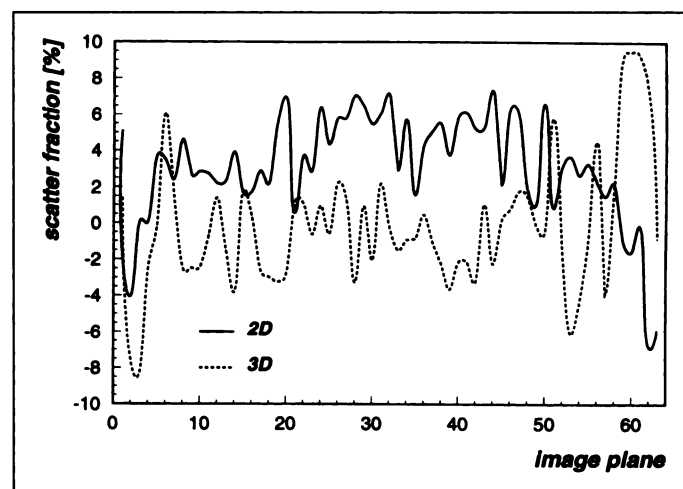


FIGURE 11. Relative scatter fraction (cf. Eq. 6) measured for all image planes after scatter correction in two-dimensional and three-dimensional mode.

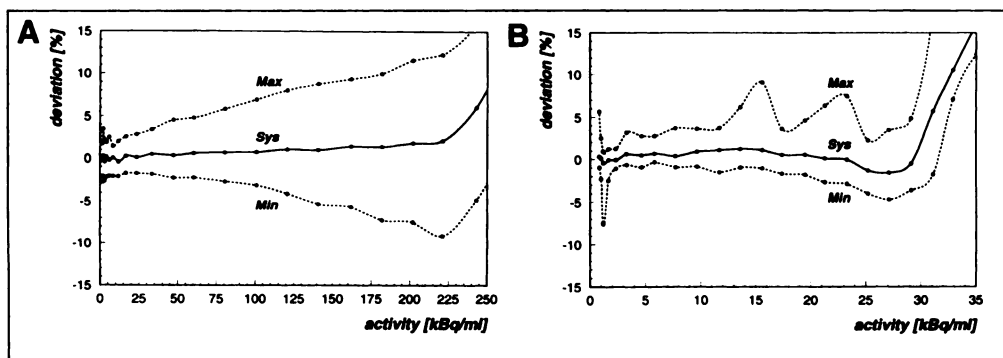


FIGURE 12. Highest and lowest percent count rate errors (cf. Eq. 7) among the 63 image planes as a function of the activity concentration. Data were obtained in (A) the two-dimensional mode and (B) the three-dimensional mode.

three-dimensional emission data were acquired over 10 min leading to a total measurement time of 50 min. Multiple regions with enhanced FDG uptake were found in the upper mediastinum and in both lungs. These lesions were interpreted as tumor recurrence and lung metastases.

Figure 15 shows four out of 63 slices of the brain for the same patient measured 95 min after [^{18}F]FDG injection. The scans demonstrate clear depiction of the deep nuclei and good gray-to-white matter contrast and visualization of cerebellar and skull base structures. Attenuation correction of the brain images was done analytically, applying the tool incorporated in the ECAT software.

DISCUSSION

The overriding concern of the applied NEMA protocol is to establish a standard to characterize the physical performance of PET scanners in order to compare performance and to understand the abilities and limitations of the scanner for use in patient studies (1,2,8). To our knowledge, this paper presents the first two-dimensional and three-dimensional performance evaluation strictly after the revised version of the NEMA protocol from 1994 (2). Since the choice of the acquisition parameters, which are not exactly defined by the standard (such as the energy window, the settings for span and ring acceptance, etc.), is somewhat arbitrary (9), we followed the instruction of the NEMA protocol "to choose acquisition parameters as they would be set for a patient study." The parameters used in our study for all performance measurements were optimized and recommended by the manufacturer for patient examinations. Moreover, they are comparable to a certain extent to those used in the performance evaluation of two other modern volume PET scanners commercially available today: the ECAT EXACT HR (Siemens/CTI) (10) and the Advance (General Electric Medical Systems, Milwaukee, WI) (11).

A drawback of the current version of the NEMA standard is that the protocol does not give clear instructions on how to evaluate the sinograms obtained in the three-dimensional mode. The 239 sinograms acquired in a single three-dimensional

emission scan can either be analyzed individually or can be single-slice rebinned before data evaluation, which means that all events are assigned to the transverse slice passing through the midpoint of the corresponding LOR. In this study, the first approach was used in order to avoid manipulations on the raw data as far as possible. Due to the resulting large number of sinograms, however, we did not plot individual data for each of the 239 sinograms as required by the NEMA protocol for some measurements. The data presented in Figures 4 and 7, for example, show only the results for the 63 nonoblique sinograms, i.e., for the central segment of the Michelogram (Fig. 1B). However, system or volume parameters were derived by using all sinograms.

Another problem resulted from the fact that in most of the performance tests, we were not able to fulfill, on the one hand, the protocol requirements concerning the total number of net true events and, on the other hand, the condition that the initial activity should be less than that at which either the percent dead-time losses and the random coincidence rate exceeds a given limit of the total event rate. Since this is a general problem using PET scanners with block detectors, we suggest that the relevant guidelines should be adjusted in a future revision of the NEMA protocol. In our measurements, we preferred to exceed the upper limit of the random coincidence rate in order to follow the guideline concerning the total number of counts. This is justified by the fact that random events can be corrected very accurately by measuring the event rate occurring in a delayed coincidence time window.

The most important novel feature of the ECAT EXACT HR⁺ is the fine axial sampling distance of 2.4 mm, which is almost identical to the transaxial sampling. This results in a nearly isotropic resolution of better than 6 mm within a FOV of 20 cm at the FWHM level, which allows reslicing of the data in any arbitrary direction without visible artifacts (cf. Fig. 14). If necessary, i.e., for small animal studies, the axial slice width can be further improved by choosing a smaller acceptance angle (cf. Fig. 2A) at the price of a substantially

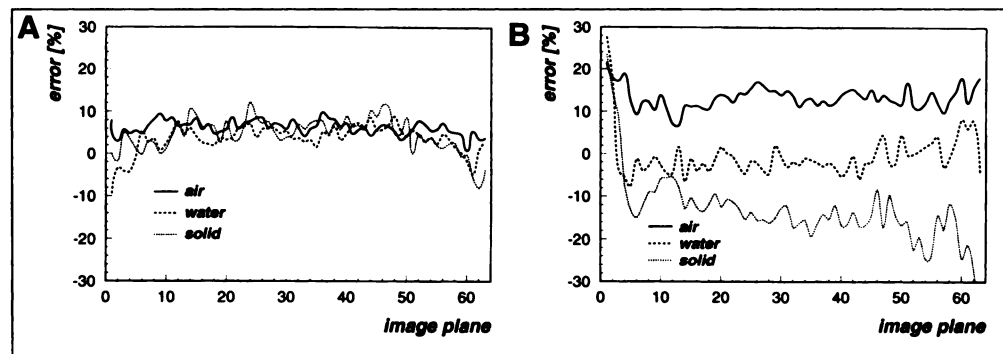


FIGURE 13. Remnant attenuation errors (cf. Eq. 8) estimated for the three inserts (air, water and solid) placed in the performance phantom for each image plane in (A) the two-dimensional mode and (B) the three-dimensional mode.

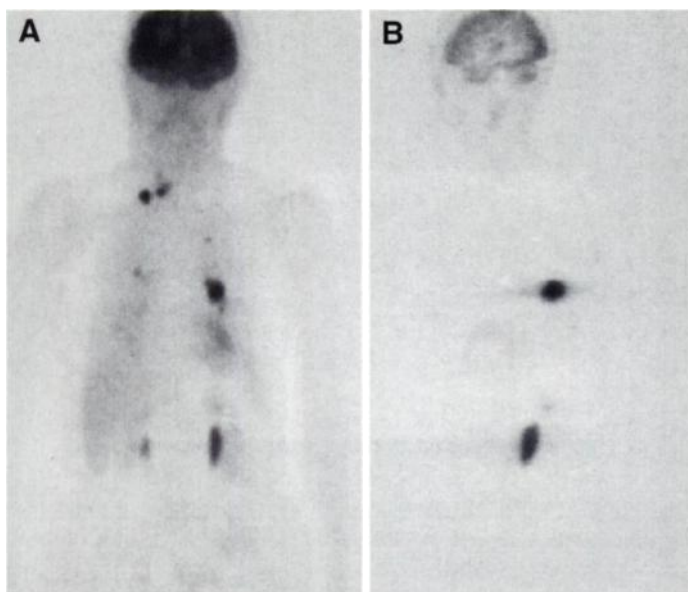


FIGURE 14. Female patient with follicular thyroid carcinoma (pT2NxMx) 2 yr after surgical resection and two radioiodine therapies with 8 GBq ^{131}I total. Beginning 40 min after the injection of 460 MBq of [^{18}F]FDG, emission data were acquired over 50 min and reconstructed without scatter and attenuation correction using a ramp filter with a cutoff at the Nyquist frequency. (Left) Coronal projection image and (right) sagittal plane through the lung metastasis in the left caudal lobe.

reduced slice sensitivity. A decrease of the span factor in the two-dimensional mode from 15 to 3, for example, results in a reduction in the true event sensitivity by a factor of about 3 (12). Thus, the fine axial sampling realized at the ECAT EXACT HR⁺ scanner cannot be used in clinical routine for patient examinations in the two-dimensional mode. However, it may be very advantageous for fully three-dimensional image reconstruction. The transaxial resolution measured in our study is compatible with the results presented for other PET scanners using BGO block detectors (10,11,13–15), as well as with the empirical formula suggested by Moses and Derenzo (16).

One of the most important problems in three-dimensional PET imaging is the tremendous amount of scattered radiation. For the ECAT EXACT HR⁺, the removal of the septa increases the average scatter fraction from about 17% (two-dimensional) to 33% (three-dimensional). Considering the different length of septa, both values agree well with results obtained from other scanners with retractable septa operating at a comparable energy window (10,11,14,17). Our phantom measurements also validate the accuracy of the implemented two-dimensional and three-dimensional scatter correction algorithm.

The favorable properties of the simulation-based three-dimensional scatter correction algorithm make it possible to measure without the shadowing effect of interslice septa and thus to use larger acceptance angles to increase the number of accepted events. Using the standard settings for span and ring acceptance results in an increase of the total true event sensitivity by a factor of about 4.9 (5.7 versus 27.7 cps/Bq/ml). It is important to note, however, that the increase in sensitivity is not spread uniformly across the FOV but is peaked toward the center of the tomograph (17). Moreover, the approximation of grouping lines within the predefined acceptance angle into a single LOR causes the resolution of the scanner to blur away from the center. In most clinical situations, however, the blurring that occurs at reasonable acceptance angles is tolerable,

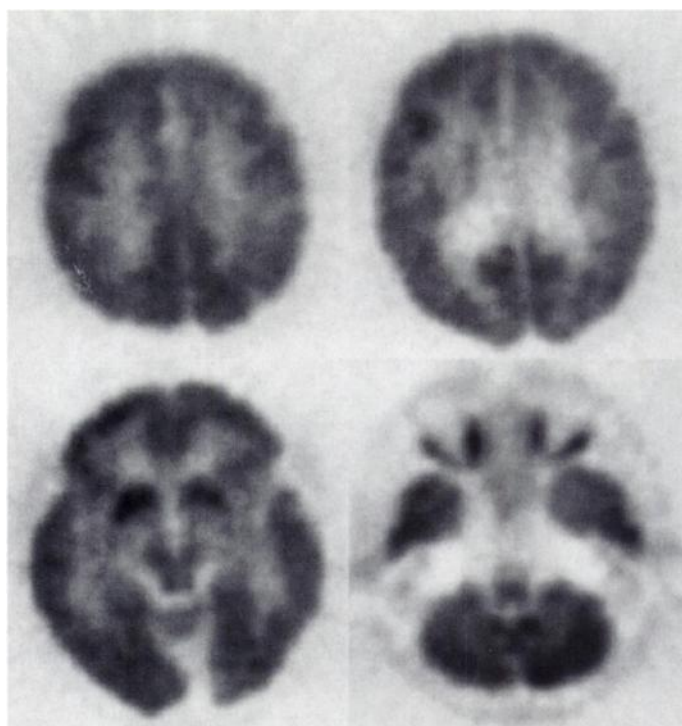


FIGURE 15. Four representative slices of a 20-min three-dimensional brain emission scan ($4 \cdot 10^8$ net true events) of the female patient shown in Figure 14. The measurement was started 95 min after injection of 460 MBq of [^{18}F]FDG. After performing a scatter and an analytical transmission correction, emission scans were reconstructed with a matrix size of 128×128 and a pixel size of $1.4 \times 1.4 \text{ mm}^2$ using a ramp filter with a cutoff at the Nyquist frequency.

since the detector ring is significantly larger than the patient port.

The volume sensitivity of a PET system is primarily determined by the total solid angle and the lower energy threshold. If energy threshold, total axial detector length and detector thickness are kept constant, sensitivity varies approximately with the inverse of the diameter of the detector ring. Based on this consideration, the system sensitivity of our PET system fits to the results obtained with other recently developed BGO-based whole-body PET scanners (10,11). It should be noted that the sensitivity numbers given in this paper do not contain the scatter contribution in agreement with the revised NEMA protocol.

All measured count rate curves shown in Figure 5 demonstrate a relatively sharp bend at a specific activity of about 180 kBq/ml in the two-dimensional mode and at 27 kBq/ml in the three-dimensional mode. In contrast to the two-dimensional mode, there is a sharp maximum of the true curve in the three-dimensional mode. Comparing our results with those obtained by Wienhard et al. for the ECAT EXACT HR⁺ (10), which uses detector blocks of the same volume, we conclude that the discontinuities observed in the count rate curves of the ECAT EXACT HR⁺ scanner are due to the acquisition control system (ACS II) and not due to the detector blocks. The count rate behavior of the true events measured in the three-dimensional mode suggests that by improving the ACS II, a maximum count rate of approximately 350 kcps may be achieved at an activity concentration of about 35 kBq/ml. The implemented correction methods for dead-time losses and random events yield very accurate results over the relevant range of activity concentrations.

CONCLUSION

The newly designed ECAT EXACT HR⁺ scanner provides an excellent spatial resolution, which can advantageously be used for brain, heart and small animal studies. Whereas the relatively low slice sensitivity may hamper the capability for performing fast dynamic studies in the two-dimensional mode (e.g., H₂[¹⁵O] studies), the scanner offers a sufficient sensitivity and count rate capacity for fully three-dimensional whole-body imaging.

ACKNOWLEDGMENTS

We thank the personnel of the cyclotron and the radiochemistry group for providing the activated ⁶⁴Cu sources and ¹⁸F-labeled agents used in this study, as well as the personnel of the workshop for technical support.

REFERENCES

1. Karp JS, Daube-Witherspoon ME, Hoffman EJ, et al. Performance standards in positron emission tomography. *J Nucl Med* 1991;12:2342-2350.
2. *NEMA Standards Publication NU 2-1994*. National Electrical Manufacturers Association, 1994.
3. Kinahan P, Rogers JG. Analytical three-dimensional image reconstruction using all detected events. *IEEE Trans Nucl Sci* 1989;36:964-968.
4. Casey ME, Gadagkar H, Newport D. A component-based method for normalization in volume PET. In: *Proceedings of the 1995 International Meeting on Fully Three-Dimensional Image Reconstruction in Radiology and Nuclear Medicine* 1995:61-65.
5. Bergström M, Eriksson L, Bohm C, Blomqvist G, Litton J. Correction for scattered radiation in a ring detector positron camera by integral transformation of the projections. *J Comput Assist Tomogr* 1983;7:42-50.
6. Hoverath H, Kuebler WK, Ostertag HJ, et al. Scatter correction in the transaxial slices of a whole-body positron emission tomograph. *Phys Med Biol* 1993;38:717-728.
7. Watson CC, Newport D, Casey ME. A single scatter simulation technique for scatter correction in three-dimensional PET. In: Grangeat P, Amans JL, eds. *Three-dimensional image reconstruction in radiology and nuclear medicine*. Dordrecht, The Netherlands: Kluwer; 1996:255-268.
8. Karp JS, Muehllehner G. Standards for performance measurements of PET scanners: evaluation with the UGM PENN-PET 240H scanner. *Med Prog Technol* 1991;17:173-187.
9. Bice AN, Miyaoka RS. Standardized tests of PET performance. *J Nucl Med* 1992;33:1429-1430.
10. Wienhard K, Dahlbom M, Eriksson L, et al. The ECAT EXACT HR⁺ performance of a new high resolution positron scanner. *J Comput Assist Tomogr* 1994;18:110-118.
11. DeGrado TR, Turkington TG, Williams JJ, Stearns CW, Hoffmann JM, Coleman RE. Performance characteristics of a whole-body PET scanner. *J Nucl Med* 1994;35:1398-1406.
12. Adam LE, Zaers J, Ostertag H, et al. Performance evaluation of the PET scanner ECAT EXACT HR⁺. In: Karp J, ed. *IEEE 1996 NSS and MIC Conference Record*; in press.
13. Rota Kops E, Herzog H, Schmid A, Holte S, Feindeggen LE. Performance characteristics of an eight ring whole body PET scanner. *J Comput Assist Tomogr* 1990;14:437-445.
14. Wienhard K, Eriksson L, Grootoonk S, Casey M, Pietrzyk U, Heiss WD. Performance evaluation of the positron scanner ECAT EXACT. *J Comput Assist Tomogr* 1992;16:804-813.
15. Townsend DW, Wensveen M, Byars LG, et al. A rotating PET scanner using BGO block detectors: design, performance and applications. *J Nucl Med* 1993;34:1367-1376.
16. Moses WW, Derenzo SE. Empirical observation of resolution degradation in positron emission tomographs utilizing block detectors. *J Nucl Med* 1993;34:101P.
17. Cherry SR, Dahlbom M, Hoffmann EJ. Three-dimensional PET using a conventional multislice tomograph without septa. *J Comput Assist Tomogr* 1991;15:655-668.

Improved Resolution for PET Volume Imaging through Three-Dimensional Iterative Reconstruction

Jeih-San Liow, Stephen C. Strother, Kelly Rehm and David. A. Rottenberg

PET Imaging, Veterans Administration Medical Center; Departments of Radiology and Neurology, University of Minnesota, Minneapolis, Minnesota

It has been demonstrated that in two-dimensional iterative reconstruction, a resolution model can improve image resolution while controlling noise. With the lower noise levels of three-dimensional PET volume imaging, these iterative reconstruction advantages may be extended to three dimensions to further improve the reconstructed image resolution. **Methods:** We have implemented three-dimensional versions of iterative filtered backprojection (IFBP) and the maximum likelihood by expectation maximization (ML-EM) reconstruction algorithms and applied them to three-dimensional PET volume datasets. The results were compared to images obtained using the standard three-dimensional reprojection reconstruction (3DRP) algorithm. **Results:** For IFBP with 15 iterations and no regularization compared to 3DRP, both using a ramp filter, the transaxial resolution improved 52%, and the axial resolution improved 39%. With a strong regularization, the transaxial and axial resolution improvements were reduced to 6% and 5%, respectively. If a Hanning roll-off is applied to the ramp filter in the transaxial direction, the transaxial resolution for IFBP without regularization improved 35% compared to 3DRP; with regularization the improvement dropped to 19%. The axial resolution for IFBP and 3DRP was unaffected by this transaxial smoothing in the reconstruction filter. With the same Hanning roll-off, the noise for IFBP without regularization increased by a factor of 6 compared to 3DRP; with regularization the noise was increased only by a factor of 3. Compared to IFBP, the three-dimensional ML-EM reconstruction produced simi-

lar resolution improvements with a much smaller increase in noise and slower convergence. Resolution improvements from both IFBP and ML-EM reconstructions are visually apparent in three-dimensional FDG brain images and result in increased activation signals in a three-dimensional [¹⁵O]water functional activation study. **Conclusion:** Our results demonstrate that resolution improvement is possible for IFBP and ML-EM compared to 3DRP with or without noise increase.

Key Words: PET; three-dimensional volume imaging; iterative reconstruction; resolution improvement

J Nucl Med 1997; 38:1623-1631

The removal of interplane septa to allow off-plane coincidences to be collected for multi-ring detectors has increased the sensitivity of PET cameras (1,2). This increased sensitivity is especially useful in studies where the required frame duration is short, the tracer used has a short half-life, or the tracer uptake is limited and confined to small regions within the scanning field of view (3). However, there are two drawbacks to three-dimensional PET volume imaging (PVI). First, the oblique penetration of photons in the detectors degrades the axial resolution compared with two-dimensional imaging with the septa extended (3,4). Second, the standard three-dimensional filtered backprojection reconstruction (the three-dimensional reprojection algorithm (3DRP) (5)) is based on forward projecting a low-statistics two-dimensional image volume to estimate the missing part of the truncated projections, followed by a full

Received Mar. 29, 1996; revision accepted Oct. 23, 1996.

For correspondence or reprints contact: Jeih-San Liow, PhD, PET Imaging (11P), VA Medical Center, One Veterans Dr., Minneapolis, MN 55147.